

An investigation of single sand particle fracture using X-ray micro-tomography

B. ZHAO*, J. WANG*, M. R. COOP*, G. VIGGIANI† and M. JIANG‡

Particle breakage is of fundamental importance for understanding the mechanical behaviour of sands and is relevant to many geotechnical engineering problems. In order to gain new insights into the mechanism of breakage of individual sand particles under single-particle compression, this study combines mechanical tests with three-dimensional X-ray micro-computed tomography (μ CT) performed ‘in situ’, that is, during loading. A novel mini-loading apparatus was developed to perform in-situ compression tests within a laboratory nanofocus X-ray CT. The tests were performed on eight particles, four Leighton Buzzard sand (LBS) particles and four highly decomposed granite (HDG) particles, to study their different fracture mechanisms. A series of image processing and analysing techniques was utilised to obtain both qualitative and quantitative results. The most important factors in determining the fracture patterns of the LBS and HDG particles were found to be particle morphology and initial microstructure, respectively. Versatile fracture patterns deviating from simple vertical splitting were observed, particularly in HDG particles. The change of morphology parameters during loading was found to depend on the fracture mechanisms and material properties, independently of their initial values. The fragments of both the LBS and HDG particles satisfy the fractal distribution, which indicates that the fragmentation is scale invariant. Different energy dissipation mechanisms were found. The energy dissipation by friction gradually prevails against the energy dissipated in generating new surfaces.

KEYWORDS: fractals; laboratory tests; particle crushing/crushability; particle-scale behaviour; sands

INTRODUCTION

Particle breakage plays an important role in determining the constitutive behaviour and deformation characteristics of granular materials, especially at high stress levels. For one-dimensional compression, particle breakage was found to be the principal source of plastic volumetric compression on the normal compression line (McDowell & Bolton, 1998), and a strong correlation was found between single-particle crushing strength and the macroscopic yield stress of sand (McDowell, 2002; Yoshimoto *et al.*, 2012). In triaxial tests, the dilatant behaviour of crushable soils was found to be governed by the tensile strength of particles (McDowell & Bolton, 1998; Yoshimoto *et al.*, 2012). The successive breakage of soil particles tends to form a fractal particle size distribution, which gives a linear distribution on a double logarithmic graph (McDowell *et al.*, 1996; McDowell & Bolton, 1998; Coop *et al.*, 2004; McDowell, 2005; Tarantino & Hyde, 2005; Russell, 2011).

Displacement-controlled single-particle compression tests, in which individual particles are compressed between two rigid platens, are often used to measure the strength of sand particles and other granular materials. Single-particle compression tests have been performed on sand particles with a wide range of particle sizes and mineral types (Lee, 1992; Nakata *et al.*, 1999; McDowell, 2002; Cil & Alshibli, 2012; Cavarretta *et al.*, 2010). The particle fracture phenomenon

has also been investigated by analytical models (e.g. Cavarretta & O’Sullivan, 2012). This test provides important information for calibrating discrete-element method (DEM) modelling of crushable sand particles. Some DEM researchers have used crushable aggregates that were composed of spherical particles cemented at their contact points (Robertson, 2000; McDowell & Harireche, 2002; Bolton *et al.*, 2008; Hanley *et al.*, 2011; Wang & Yan, 2012, 2013; Cil & Alshibli, 2012, 2014), whereas Lobo-Guerrero & Vallejo (2005) implemented a different particle fracture approach involving the replacement of a rigid particle with a group of smaller particles based on a certain tensile failure criteria. Physical tests, analytical methods and numerical simulations have all been used to understand the relationship between the load–deformation response of individual particles and the overall stress–strain response of a granular material (McDowell & Bolton, 1998; Nakata *et al.*, 1999, 2001; Cheng *et al.*, 2003; Russell & Einav, 2013). However, limited studies have been conducted to understand the relationship between single-particle fracture and particle external morphologies and internal microstructure (e.g. cleavage, impurities and voids) owing to experimental difficulty in examining the evolution of particle microstructure during the fracture process.

X-ray micro-tomography provides a powerful tool for dealing with the above difficulty. A rich body of studies have been conducted on the deformation and fracture mechanisms of a wide range of materials including biological materials (e.g. tissues and bones), construction materials (e.g. ceramics, asphalt and rock), composite materials, synthetics and cellular solids (Stock, 2008). For granular soils, X-ray tomography was first used to investigate strain localisation in triaxial tests (Desrues *et al.*, 1996; Alshibli *et al.*, 2000). These studies demonstrated that X-ray tomography is an effective tool for observing the localisation patterns and quantifying the evolution of void ratio inside a shear band.

Manuscript received 18 August 2014; revised manuscript accepted 16 April 2015.

Discussion on this paper closes on 1 January 2016, for further details see p. ii.

* Department of Architecture and Civil Engineering, City University of Hong Kong, Hong Kong, China.

† University Grenoble Alpes, Grenoble, France.

‡ Department of Geotechnical Engineering, Tongji University, Shanghai, China.

Early studies used a voxel size of hundreds of microns that did not accurately resolve the particles. More recently, a number of studies on granular materials have been conducted with much better resolution (a few microns), allowing grain-scale characterisation of sand deformation under load (e.g. Andò *et al.*, 2013). Grain-scale observations enrich our understanding with the full kinematics (i.e. three-dimensional (3D) displacements and rotations) of all the individual sand grains in a specimen (Hall *et al.*, 2010), the evolution of 3D particle morphology and fabric of a real sand under loading (Fonseca *et al.*, 2012, 2013), and the evolution and distribution of particle breakage (Andò *et al.*, 2013; Cil & Alshibli, 2014). The fracture of silica sand particles has been examined experimentally with 3D synchrotron tomography and numerically with 3D DEM simulations simultaneously (Cil & Alshibli, 2012, 2014).

The objective of this paper is to explore the fracture process of the sand particles under single-particle compression using micro-computed tomography (μ CT) and crushing tests. A novel in-situ single-particle compression apparatus was developed and used to carry out crushing tests on two kinds of sand particles, namely Leighton Buzzard sand (LBS) particles and highly decomposed granite (HDG) particles. The μ CT scanning of the particles was carried out while they were loaded. A series of image-processing and analysis techniques were then applied to the 3D CT images of the particles to yield knowledge of the particle fracture behaviour at both qualitative and quantitative levels, the former containing information of fracture patterns and microstructure evolution and the latter giving statistics of fragment morphology. This information offers novel insights into the relationship between single-particle fracture behaviour and the intrinsic particle microstructure. The breakage energy, which was evaluated by using the load–displacement curve and the measured surface area of the particle fragments, provides further valuable information of the fracture mechanics of sand particles.

EXPERIMENTAL SET-UP

A mini-loading apparatus was designed to perform single-particle crushing tests on natural sand particles in a laboratory μ CT system (v|tome|x m, phoenix|X-ray, General Electric Company (GE)) located at Shanghai Yinghua NDT Equipment Trade Co., Ltd. A 3D scheme and a photograph of the apparatus in operation are shown in Fig. 1. The apparatus consists of three major parts: the sample chamber, the loading and data acquisition system and the bearing frame.

The sample chamber, located in the top part of the apparatus, is a high-strength radiolucent tube made of polyetherimide (PEI). With its high strength, the PEI tube can be long and thin enough to let the GE nanofocus X-ray tube get close to the sand particle to reach the highest CT resolution. The PEI tube is 105 mm long, and has a 22 mm outer diameter and a 10 mm inner diameter. Inside the PEI tube, the sand particle is loaded between two ceramic platens. The loading platens are made of ceramic owing to its low density (3.85 g/cm^3), whereas carbon steel has a density of 7.85 g/cm^3 . A sharp change of linear attenuation coefficient from the particle to the loading platens will greatly increase the cone beam errors (Davis & Elliott, 2006). Therefore, lower density platens can reduce the amount of blurring on the CT images, especially around the contact points. According to the theoretical work by Russell & Muir Wood (2009), Young's modulus, Poisson ratio, hardness and roughness of the loading platens can all have effects on the actual contact area and thus the stress distribution and fracture mechanisms of the particle. In an effort to minimise

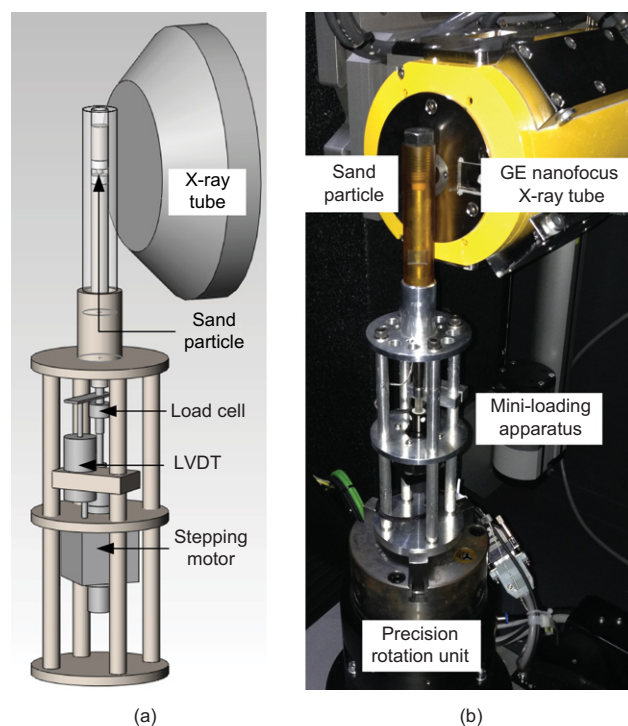


Fig. 1. Close-up of the mini-loading apparatus: (a) 3D view of the apparatus; (b) photograph of apparatus in operation inside X-ray machine (GE, General Electric Company)

any such effect, the present authors selected a ceramic platen with a high Young's modulus of 380 GPa, a high hardness of 1700 HV (HV is the Vickers pyramid number), a low Poisson ratio of 0.22 and a low roughness of $R_a = 0.2 \mu\text{m}$. After the test, no plastic deformation (i.e. breaking of asperities) was identified from the CT images. Therefore, it is believed that the ceramic platens had little influence on the particle fracture and energy dissipation mechanisms. In order to prevent fragments from jumping out of the scanning area and to maintain the fracture patterns during scanning, the sand particle is immersed in high-viscosity silicone grease during the test.

The force is exerted on particles by a microstep linear actuator (NA14B16-T4-MC04, Zaber Technologies Inc.), which is capable of exerting a force up to 222 N with a microstep size of $0.09525 \mu\text{m}$. The exerted force is measured by a miniature load cell (Model 111, Sensorwerks) with dimensions small enough to fit inside the apparatus. This load cell is rated for 222 N with a non-linearity of 1.33 N and non-repeatability of 2.66 N. A linear variable differential transformer (LVDT) (DFg 2.5, Solartron Metrology), rated for a range of $\pm 2.5 \text{ mm}$ with an infinite resolution and non-linearity of $\pm 7.5 \mu\text{m}$, is used to measure the displacement of the loading platen. In order to review the load and displacement signals, a model 7220 (Measurement Systems Ltd) direct current (DC) measurement processor with 16-bit resolution is used. The linear actuator and measurement processor are controlled by specially written in-house software that allows for running both displacement- and load-controlled tests.

The PEI tube is screwed onto the bearing frame, the base of which is fixed onto a precision rotation unit by way of a three-jaw chuck (Fig. 1(b)). The precision rotation unit rotates the apparatus and the sample 360° to finish one scan. During each scan, the linear actuator stops while the load cell and the LVDT keep recording the force and displacement.

MATERIALS TESTED

In this study, two types of natural sand particles with different morphology, mineralogy and microstructure were tested. Considering the load capacity of the apparatus (linear actuator and load cell) and the resolution of the CT scanning, particles with dimensions between 1.2 and 2.0 mm were used, which were selected randomly. LBS particles are mainly composed of quartz, which is chemically stable. Their shape and surface texture are mainly modified by the geological transportation process. Fig. 2(a) shows a microscopic view of a typical LBS particle with a high degree of roundness and a smooth surface. The Geotechnical Control Office (1984) proposed six granite weathering grades, namely fresh rock, slightly decomposed rock, moderately decomposed rock, highly decomposed rock, completely decomposed rock and residual soil. HDG particles, corresponding to the fourth weathering level, were used in this study. It is granitic rock weathered to the point that it readily fractures into pieces that can be broken by hand. They are composed of feldspar, quartz, mica and other minerals. At this weathering grade, plagioclase has been almost completely altered to clay minerals and the formation of dissolution features, such as pits, trenches and channels, could be observed in the alkali feldspar. Kaolin and micaceous minerals represent 10 to 30% in mass. Fig. 2(b) shows a microscopic view of a typical HDG particle, which has a larger angularity and more complex mineralogy than the LBS particles.

Although μ CT imaging is a very powerful tool for visualising 3D structures, it can be difficult to identify

different phases because it is based on X-ray linear attenuation coefficients. Scanning electron microscopy (SEM) and energy-dispersive X-ray spectroscopy (EDS) were used to identify the different minerals from the surface of the HDG particles, and this information was then used to interpret the μ CT images. Fig. 3(a) shows two minerals (quartz and feldspar) and a micro-crack between these two phases, while Fig. 3(b) shows both feldspar and its weathering products.

IMAGE ACQUISITION, PROCESSING AND ANALYSIS

The image acquisition was conducted using a Phoenix v|tome|x m, in which the samples are radiated with a high-resolution nanofocus X-ray beam (180 kV/15 W). Each sample was scanned rotating the apparatus 360° around its central axis between an X-ray tube and a detector. The detector has 2000 × 2000 pixels. A series of absorption radiographs of the sample were acquired during the step-wise rotation of the apparatus. The 3D volume reconstruction was achieved using Phoenix Datos|x CT, a software using the Feldkamp filtered back projection algorithm. The voxel size of these reconstructed images is 3.3 μ m when the X-ray tube is closest to the PEI tube. The effective scanning volume is a cylinder with both height and diameter being 6.6 mm (the voxel size × number of pixels). This means that the particles and fragments should stay inside this volume if it is desired to keep the same voxel size during the test. The CT data can be

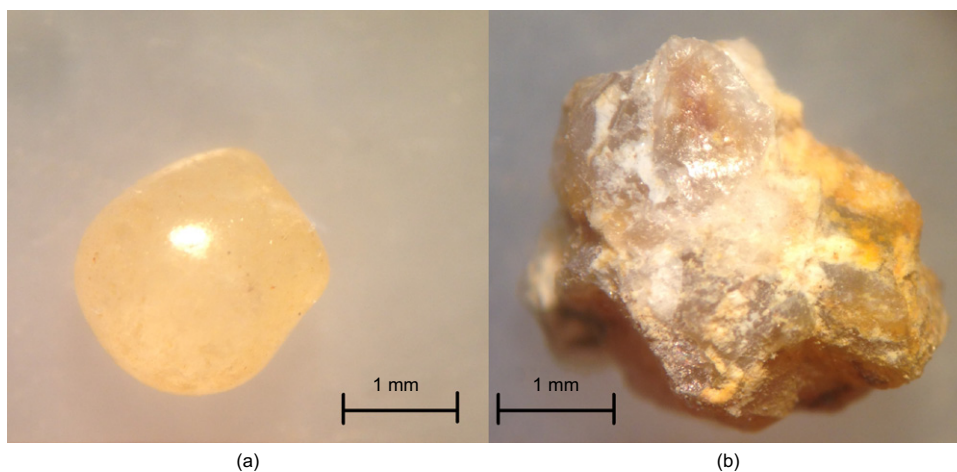


Fig. 2. Microscopic view: (a) typical LBS particle; (b) typical HDG particle

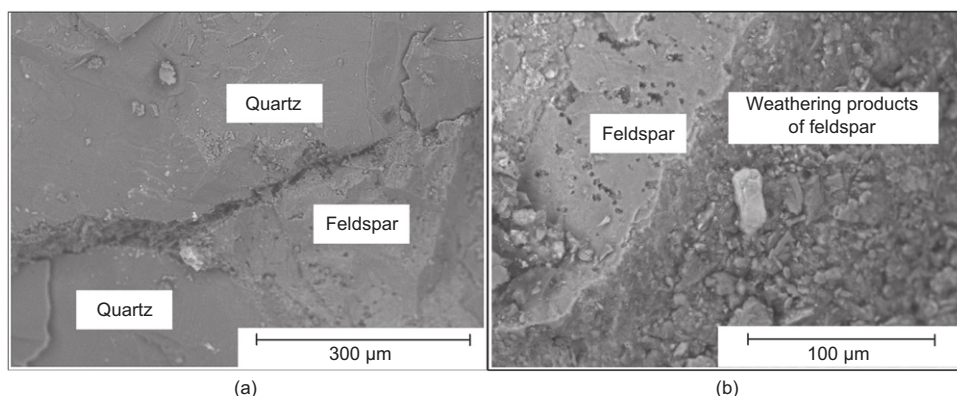


Fig. 3. SEM images of typical HDG particles: (a) initial micro-crack; (b) weathering products

visualised as a stack of images, each of which is a cross-section of the scanned sample with the thickness of one voxel size. An example of a slice is shown in Fig. 4(a).

The reconstructed 3D CT images were put through a series of image-processing and analysis procedures to obtain a qualitative and quantitative description of the particle fracture. The objective of image processing is to reduce noise, to segment different phases and to identify individual fragments. Then, image analysis techniques were implemented to measure the morphology parameters of each component. Many techniques implemented in this study have been described by Fonseca (2011) and Fonseca *et al.* (2012).

To reduce noise typically found in raw CT data, two filtering algorithms, a 3D median filter and a 3D adaptive Gaussian filter, were applied for LBS particles and HDG particles, respectively. The median filter is the best-known non-linear spatial filter, which replaces the intensity value of a voxel by the median of the intensity values in its neighbourhood (Gonzalez & Woods, 2010). The 3D median filter has a size of $3 \times 3 \times 3$, and it is repeated three times for each CT image. This method was chosen because of its excellent noise-reduction capability with considerably less blurring. However, for the CT images of HDG particles, the 3D median filter could not achieve satisfactory smoothing due to its limited filter size. In this case, the adaptive Gaussian filter, which uses a larger neighbourhood and reduces the blurring at the sharp edges, could be used

(Hodson *et al.*, 1981; Deng & Cahill, 1993; Fonseca, 2011). Fig. 4(b) shows the filtered image by the adaptive Gaussian filter with the parameters set as smoothing = 1.8 and edge threshold = 0.08. It can be seen that the image was nicely smoothed while the edges between different materials were preserved. The histogram of original image and filtered image in Fig. 4(c) shows that the intra-class variances were reduced after the filtering, which is helpful in performing the thresholding segmentation.

Then, thresholding segmentation separates the filtered images into different regions, namely, grains, silicone grease and voids, based on their representative intensity levels. Because there are more than two phases in the CT images, choosing proper thresholds based on histograms (Fig. 4(c)) was done using the intrinsic function, 'multithresh', in Matlab (Mathworks) based on the multilevel Otsu threshold method (Otsu, 1979). Generally speaking, the method divides the histogram into different classes and minimises the intra-class variances. For the filtered image (Fig. 4(b)), two threshold values were found to be 2561 and 6134, as marked in Fig. 4(c). Fig. 4(d) shows the segmented image based on these two threshold values; the three grey levels represent sand particle, silicone grease and voids, respectively. In this study, only the domain of sand particles and their fragments after fracture are of interest.

Thresholding segmentation separates the sand particles and fragments from other materials, but individual fragments cannot be identified when they touch. So the

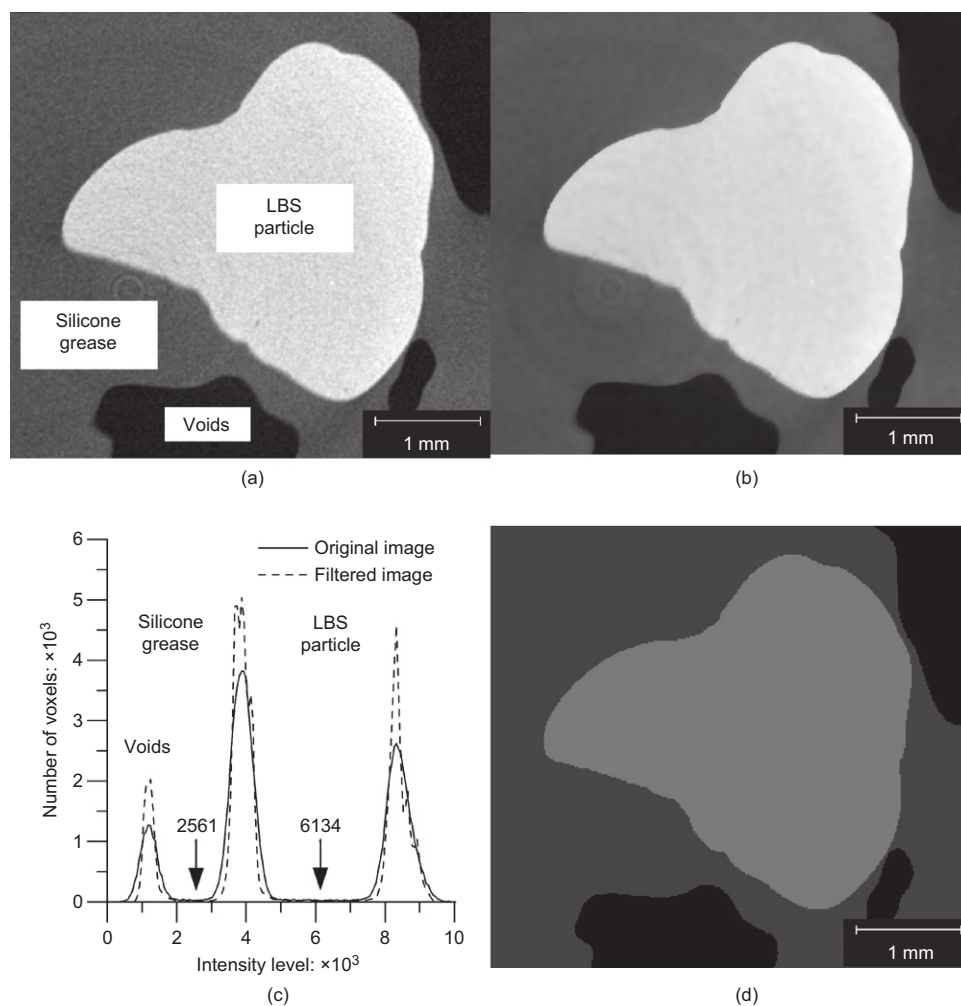


Fig. 4. Illustration of image processing: (a) raw grey image; (b) image after the 3D adaptive Gaussian filter; (c) histogram before and after filtering; (d) image after multilevel thresholding

morphological watershed algorithm (Beucher & Lantuejoul, 1979) was implemented to separate them. To illustrate the method, the segmentation process is presented here on a two-dimensional (2D) slice of a fractured particle (Fig. 5(a)) as an example, but it should be noted that the algorithms implemented in this study are 3D. Before applying the watershed algorithm, a distance map which represents the distance between each pixel and its nearest surface boundary was calculated (Fig. 5(b)). The distance map was inverted so that the maximum regions changed into minimum regions. If watershed segmentation is applied directly to the inverted distance map, it will almost always result in over-segmentation, due to the intensity variations within both the objects and background (Gonzalez & Woods, 2010). An approach based on the concept of markers was therefore used to control the over-segmentation (Wählby *et al.*, 2004). The watershed lines were determined by means of a marker-based watershed from the specified markers. Fig. 5 (c) shows the watershed lines and the binary image after removing the watershed lines. Then the fragments could be separated and labelled as different components (Fig. 5(d)). The results are the 3D labelled images, each integer in these images representing an individual fragment.

The shape of a particle can be decomposed into components in three scales, sphericity (or form), roundness (or angularity) and roughness (or smoothness) (Barrett, 1980; Cho *et al.*, 2006). The 3D digitised image data of each component allow quantitative measurement of morphology. Specifically, volume is obtained by multiplying the number of voxels defining the particle by the size of each voxel, that is, 'resol³', where resol is the spatial resolution of the image.

Surface area is estimated by a method based on the local configuration of binary valued voxels (Lindblad, 2005). In this method, each configuration is assigned a surface area weight and the total area is calculated as the sum of the local area contributions.

Principal component analysis (PCA) is applied to determine the orientation of the major, minor and intermediate axes for each component. This method has been applied to the analysis of tomographic data in different fields (Phillion *et al.*, 2008; Fonseca *et al.*, 2012). The components are rotated so that their principal axes are parallel to the Cartesian axes. The major (*a*), intermediate (*b*) and minor (*c*) dimensions of a component are then calculated by multiplying the component's voxel coordinates after rotation and the voxel size. As the data for each component are 3D, two aspect ratios are calculated, the elongation index (EI) and the flatness index (FI), which are defined as $EI = b/a$, and $FI = c/b$ ($a > b > c$). Two more parameters, namely sphericity (*S*) and convexity (C_X), are also used here to provide measures of compactness. Sphericity describes how closely a component resembles a sphere. It was originally defined as SA_{sphere}/SA , where *SA* is the surface area of the component, and SA_{sphere} is the surface area of a sphere having the same volume as the component (Wadell, 1932). Here, the sphericity *S* is calculated by way of $S = \sqrt[3]{36\pi V^2/SA}$, where *V* is the volume of the component. Convexity is defined as $C_X = V/V_{\text{CH}}$, where V_{CH} is the volume of the convex hull enclosing the component. Referring to Fig. 6, a convex hull is defined as the minimal convex surface containing all voxels of the component. A surface is convex if it contains all the line segments

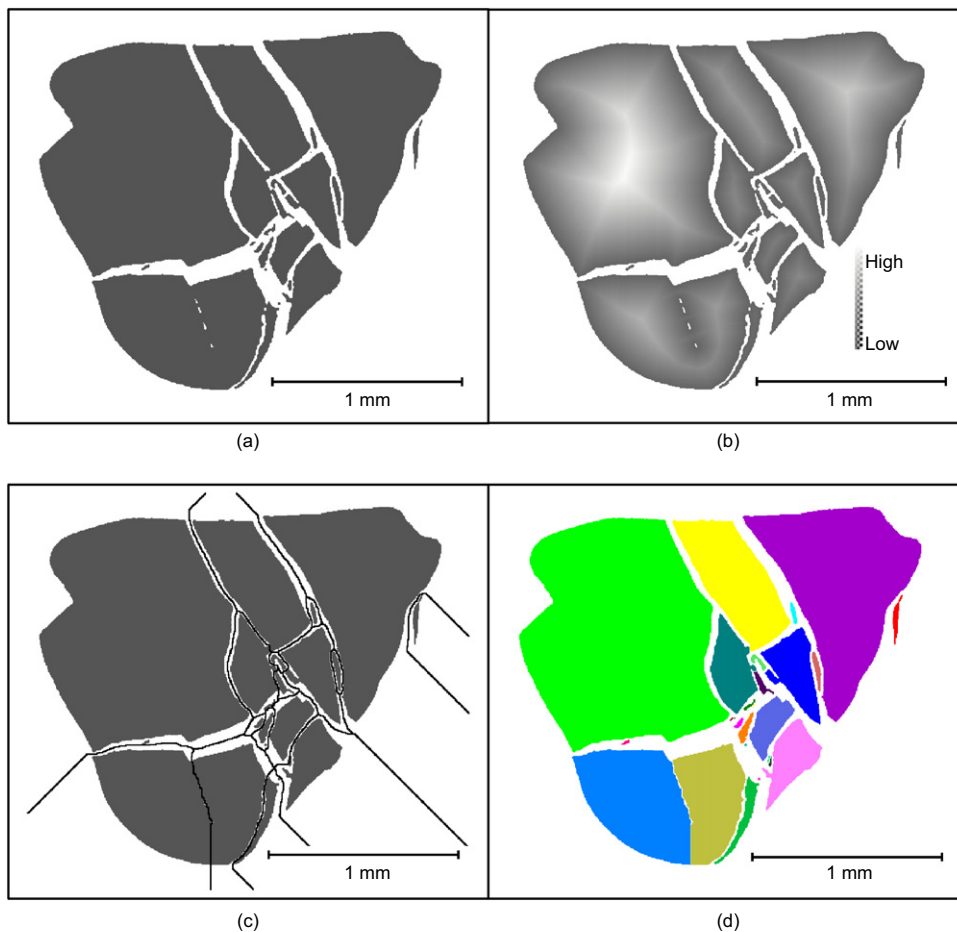


Fig. 5. Illustration of morphological watershed process on a 2D slice of fractured particle: (a) binary image after thresholding segmentation; (b) distance map; (c) watershed lines and binary image removed watershed lines; (d) labelled fragments

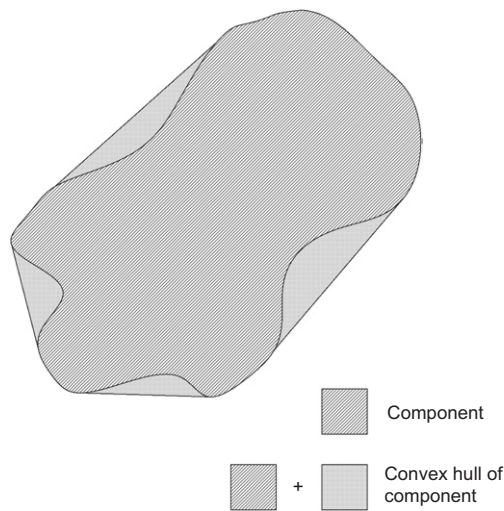


Fig. 6. Two-dimensional illustration of convex hull

connecting each pair of points inside this surface. It should be noted that the aspect ratios only reflect the form of particle shape, while S and C_X are sensitive to both roundness and form (Barrett, 1980).

RESULTS

Initial particle morphology

In the present study, in total, eight particles – four LBS particles and four HDG particles – were tested. Their morphology information is summarised in Table 1. Fig. 7 shows 3D visualisations of the tested particles. The width of a particle is defined as its minor dimension (c). The volumes of the LBS particles tested vary from 2.18 mm³ to 3.30 mm³, while the HDG particles have a wider size variation from 3.06 mm³ to 11.30 mm³. The aspect ratios of these two kinds of particles are very similar. The HDG particles are more angular than the LBS particles, which results in lower sphericity and convexity values. The sphericity values of all the particles are slightly smaller than their convexity values.

Fracture process and fracture patterns

Each particle was scanned three times, including the initial condition and two damaged conditions with the same X-ray scanning settings and the same voxel sizes. Fig. 8 shows the load–displacement curves for LBS-1 and HDG-1 and their three scanning points. Hereafter, the scans will be denoted by a code in which the test number is followed by the number of the scan (e.g. LBS-1-S2 is the second scan of test LBS-1). For the LBS particles, the first scan was taken after a compression force of around 10 N was applied to the particle to examine their initial loading positions. For HDG particles, the first

scan was performed before applying any compression, because this would have altered the initial microstructure of the particles. The second and third scans were taken after the first fracture and at a large displacement, respectively. The force–displacement curves show that during each scan (which took about 1.5 h), the changes of force and displacement were very small (e.g. the compression force reductions of LBS-1 and HDG-1 during scan 2 are both 0.95 N).

LBS-1 is selected as an example to illustrate the fracture process observed from the CT images (Fig. 9). The three columns correspond to LBS-1-S1, LBS-1-S2 and LBS-1-S3, respectively. Figs 9(a)–9(c) present the typical 2D grey-level slices of the CT images after processing by a 3D median filter. In these images, brightness is proportional to X-ray absorption. Therefore, dark regions correspond to low-density phases (voids and silicone grease), while bright regions correspond to high-density phases (ceramic platens and sand particles). It is found that the small radius of curvature at the top contact point (Fig. 9(a)) caused stress concentration and extensive fragmentation (Fig. 9(b)). The two main tensile fracture planes were parallel to the compression direction (Fig. 9(b)). The fragmentation observed in LBS-1-S3 may be caused by direct compression by the loading platens or the interaction between fragments and different fracture mechanisms; for example, tension and bending may happen here (Fig. 9(c)) (Quinn, 2007).

The CT images from LBS-1-S2 and LBS-1-S3 demonstrated that the silicon grease could successfully keep the fragments inside the scanning volume and preserve the fracture patterns. It should be noted that the fracture patterns in scan 3 might be different without silicone grease. The fractures usually have a complex spatial distribution, which is difficult to examine only from the 2D slices. The fragments are labelled with different colours and made semi-transparent so that the fracture patterns can be examined more easily (Figs 9(e) and 9(f)). Fig. 9(d) shows the condition of the contact point at the top (noted by an arrow), where there was a small radius of curvature and a concave feature nearby. The middle sections of the thresholding segmented images perpendicular to the loading direction are shown in Figs 9(g)–9(i). There were many intersecting and branching cracks, which are helpful to interpret the sequence and propagation direction of the cracks. Three cracks stopping at the intersection have been identified and marked in Fig. 9(h). The first crack of the intersecting cracks passes through the undisturbed material, and the second crack approaches and is stopped at the intersection since it is unable to traverse the previously cleaved material. Similar observations were made by Quinn (2007).

Generally speaking, sand particle fracture is a brittle fracture consisting of relatively rapid propagation of multiple cracks through a stressed material. The patterns of crack propagation and branching not only point the way back to the point where cracking starts, but can also provide information about the origin of fracture, fracture energy

Table 1. Summary of the morphology of particles tested

Particle ref.	Voxel size: μm	Width: mm	Volume: mm ³	Surface area: mm ²	S	C_X	EI	FI
LBS-1	3.89	1.36	2.18	10.11	0.80	0.90	0.87	0.70
LBS-2	3.67	1.43	2.24	10.05	0.82	0.89	0.86	0.82
LBS-3	3.31	1.43	3.16	12.24	0.94	0.98	0.90	0.74
LBS-4	3.31	1.60	3.30	13.38	0.89	0.97	0.85	0.79
HDG-1	3.57	1.44	3.06	15.59	0.67	0.82	0.86	0.68
HDG-2	3.31	2.78	11.30	49.32	0.50	0.78	0.86	0.83
HDG-3	3.31	2.09	5.46	21.86	0.68	0.84	0.90	0.84
HDG-4	3.31	1.81	6.38	27.87	0.60	0.77	0.86	0.63

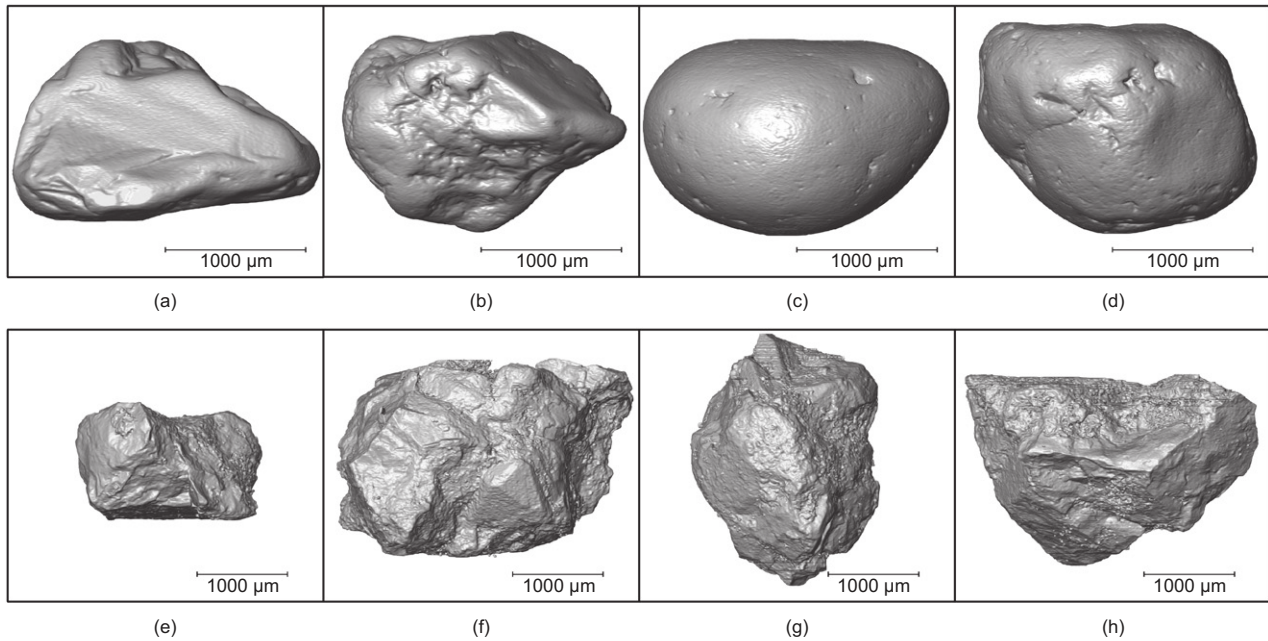


Fig. 7. Three-dimensional CT reconstruction of tested particles: (a–d) LBS-1 to LBS-4; (e–h) HDG-1 to HDG-4

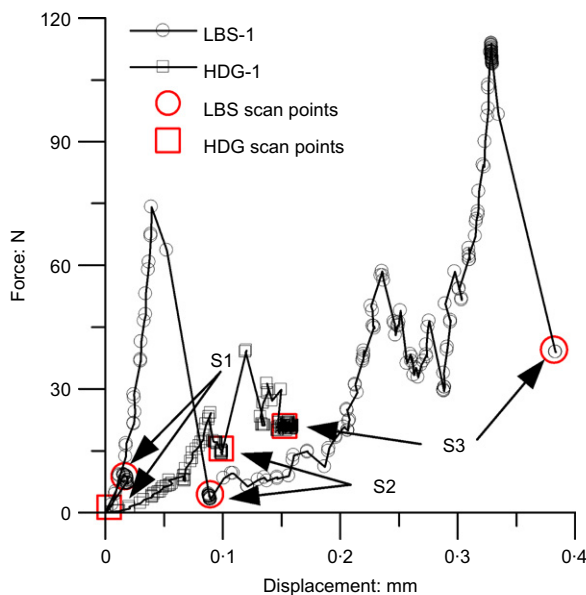


Fig. 8. Load–displacement curves from tests LBS-1 and HDG-1

and stress state (Quinn, 2007). Based on the observations of fracture patterns from CT images, it is possible either to confirm or question many hypotheses researchers have made over the years about single-particle fracture mechanisms.

The irregular morphology of natural sand particles, together with loading condition, defines the boundary conditions, influences the stress distribution inside the particle and leads to different fracture patterns. For example, the small radii of curvature near the contact points of LBS-1 and LBS-2, as shown in Figs 7(a) and 7(b), are likely to create stress concentrations. The high elastic energy stored by the stress concentrations resulted in extensive fragmentation around the contact points (Fig. 9(b)). The resulting fragments have sizes varying from around 10 μm to several 100 μm . The crushing on contact surfaces effectively increased the contact area and reduced the stress concentration at the surface. LBS-3 and LBS-4 had quite similar

fracture patterns, as shown in Fig. 10. Two planes were nearly perpendicular to each other, and separated the particle in four major fragments, as a result of tensile stress on the planes. Severe damage occurred close to the contact surfaces where the stress was mainly compressive before the fracture occurred.

The analytical solution for the stress field within an elastic sphere subject to diametrically opposite normal forces given by Russell & Muir Wood (2009) indicates that the failure will initiate somewhere directly below and close to the loading areas. This initial failure is a type of shear failure because the failure criterion used is a function of the second invariant of the deviatoric stress tensor. Although the real stress fields within the sand particles tested in the present study would differ significantly from the idealised solution given by Russell & Muir Wood (2009), mainly due to the irregular particle shapes, microstructure within particles and loading contact geometries, the validity of their solution can be roughly confirmed based on careful observation of the CT results. For example, the tensile splitting failure of LBS-1 shown in Fig. 9(b) could have started with a shear failure at a short distance below the upper loading contact, where a small fragment is found, and then propagated rapidly along the vertical plane containing the loading contacts. But this event was preceded by the severe fragmentation of the upper local contact area due to large stress concentrations, which may then make the entire stress field and hence failure mechanism within the particle drastically different from the analytical solution of Russell & Muir Wood (2009). However, it should be pointed out that the accurate identification of the initial fracture of a single particle is beyond the capability of current X-ray CT information.

X-ray CT revealed that there were some *initial* voids inside the LBS particles, especially in LBS-3 and LBS-4. These initial voids have the effect of reducing the stress needed for the development of the fracture, which results in creating a size effect in terms of particle strength (McDowell & Bolton, 1998; Nakata *et al.*, 1999; McDowell & Amon, 2000). Figs 10(c) and 10(d) show that the fracture went through some of these voids. However, it is difficult to determine, only from the CT images, whether the fracture actually started from these voids. There were also several big initial voids inside

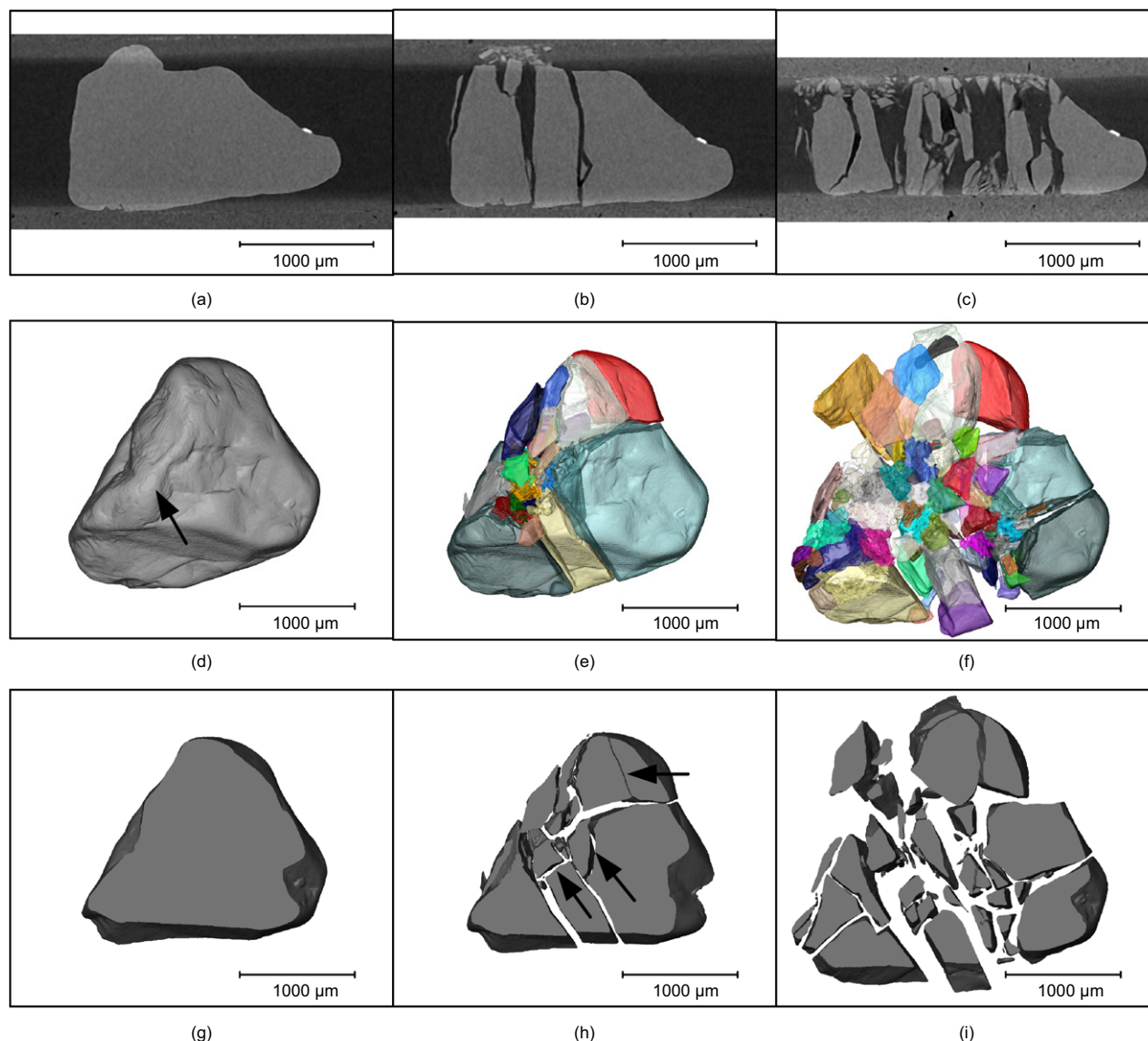


Fig. 9. Visualisation of fracture process of LBS-1 from three scans: (a–c) 2D slices parallel to the loading direction; (d–f) 3D labelled images from top view; (g–i) sections of the thresholding segmented images from top view

particle LBS-2, but the flaws remained intact after the fracture. It is possible that the stress concentrations near the contact points caused by small radii of curvature reduce the probability of fractures passing through the initial voids. Conchoidal fractures that do not follow natural planes of separation and often are curved were observed in Fig. 10(d). The above observations of the single particle fracture process are potentially valuable for the development of novel fracture mechanics models for single particle failure (e.g. Brzesowsky *et al.*, 2011).

Different kinds of initial microstructures were observed inside the HDG particles, as shown in Figs 11(a)–11(d). The two major minerals of HDG-2 shown in Fig. 11(b) are quartz (darker one) and feldspar (brighter one). This heterogeneity makes the particles much easier to break under local stress concentrations, as indicated by fractures passing through impurities of very high density (Fig. 11(e)), phases boundaries (Figs 11(f) and 11(g)) and weathering products (Fig. 11(h)). The fractures inside the feldspar show a cleavage pattern, which is caused by crystallographic planes with low bonding. For particles HDG-3 and HDG-4, the fracture disappeared in the porous weathering products from feldspar (Figs 11(g) and 11(h)).

Figure 12 and Fig. 13 present 2D slices parallel and perpendicular to the loading directions of HDG particles at three scanning points. It is found that the fracture patterns are strongly influenced by the initial microstructures that cause the structural weakness. Gallagher (1987) classified structural weakness into original structures (e.g. cleavage, remnant grain boundaries and impurities) and younger structures (e.g. fractures and solution pits). The fracture patterns shown in Fig. 12 could be divided into three groups, original fabric (OF) related, younger fabric (YF) related or independent of fabric (IF). Fracture patterns of an original fabric nature are those that are dependent on the inherent mineralogical and crystallographic structure, such as the fracture through an impurity (Fig. 13(a)) and the fractures along the cleavage of feldspar (Fig. 13(b)). Feldspar has two cleavage planes that intersect at 90°, which probably resulted in the almost perpendicular fracture planes in Fig. 13(b). Younger fabric features arise during the geological history of sand grains, such as pits and fractures that are generated by the mechanical or chemical weathering process. The younger weakness will greatly reduce the strength of the particles and completely control the induced fractures (Figs 12(c), 12(f), 12(h) and 12(k)). These types of microstructural fractures are

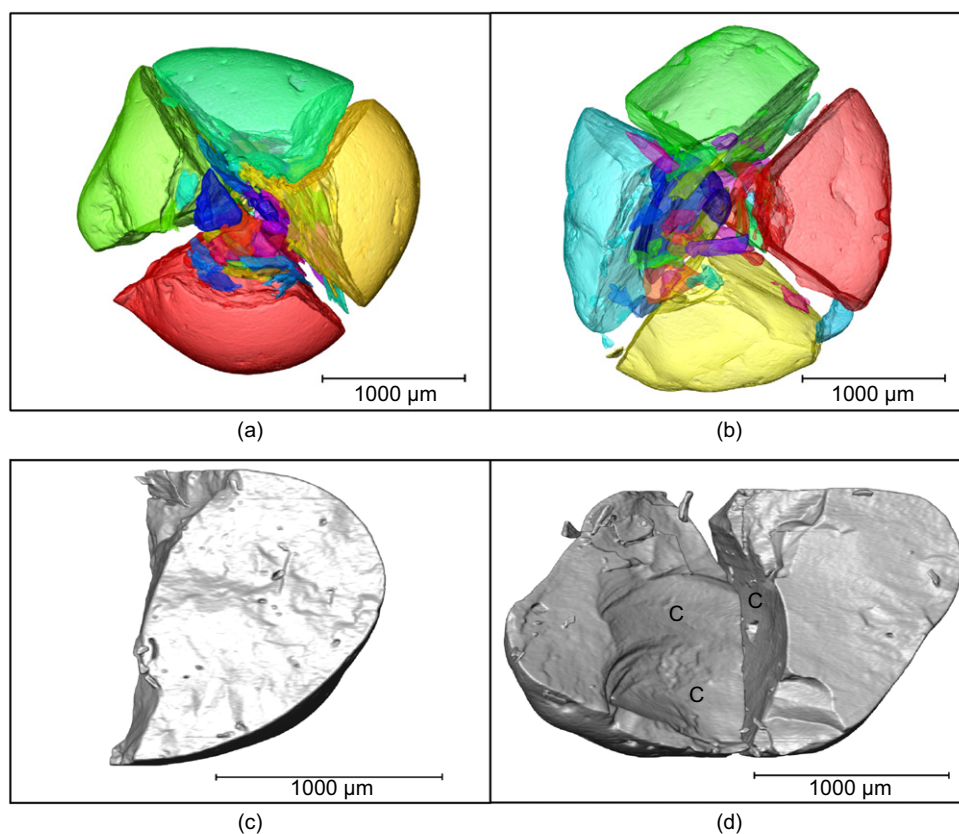


Fig. 10. Fracture patterns of LBS-3 and LBS-4: (a, b) top view of the fragments of LBS-3 and LBS-4; (c, d) fracture surface of LBS-3 and LBS-4 (C: conchoidal fractures)

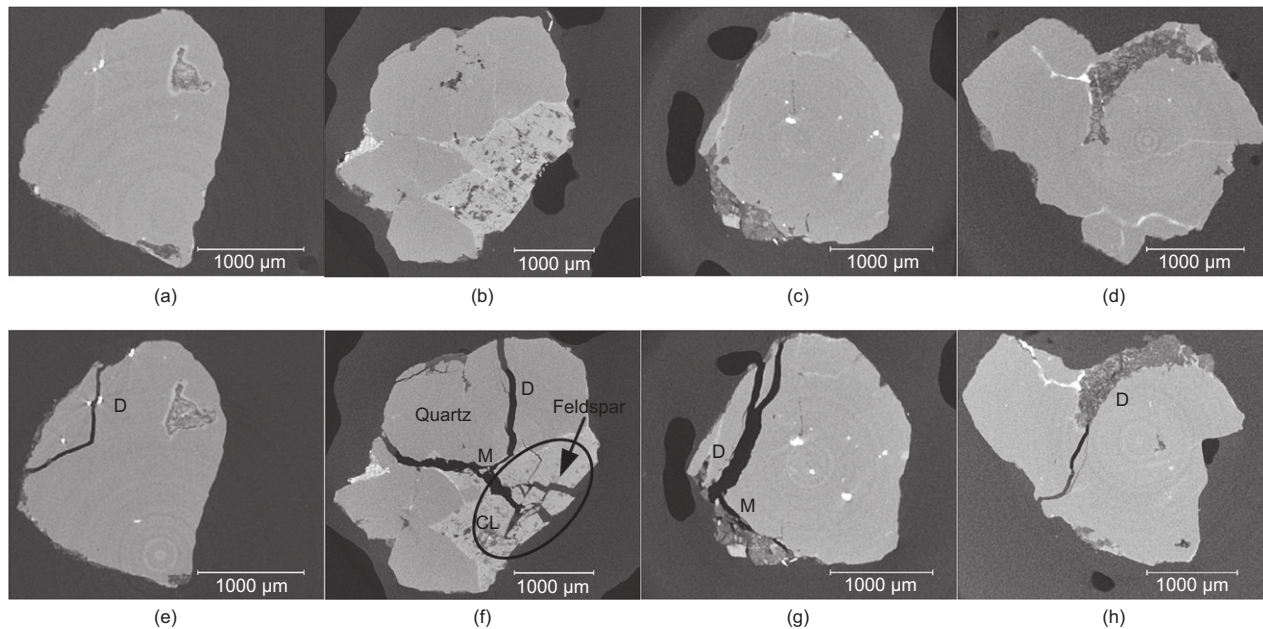


Fig. 11. Two-dimensional grey-level slices of HDG particles perpendicular to the loading directions: (a–d) HDG-1 to HDG-4 at scan 1; (e–h) HDG-1 to HDG-4 at scan 2 (CL: fractures following cleavage; D: fractures along an initial defect; M: fractures following mineral boundaries)

more frequently found in HDG that has been created by weathering, leading to particles that are more complex in mineralogy and often have internal microstructures (Lee & Coop, 1995). Fractures that are independent of structural weakness need relatively high stresses for them to be created. For example, a conchoidal fracture is a sign of fabric independent fracture (Fig. 13(a)). Conchoidal fractures are

generated in quartz because it has no cleavage. The new fractures propagating in quartz that has not been influenced by microstructural weakness are in this category and predominate in LBS, which has an almost purely quartz mineralogy from its sedimentary origin.

A bending fracture indicated by the double cantilever curl that formed when the fracture propagated from the tensile

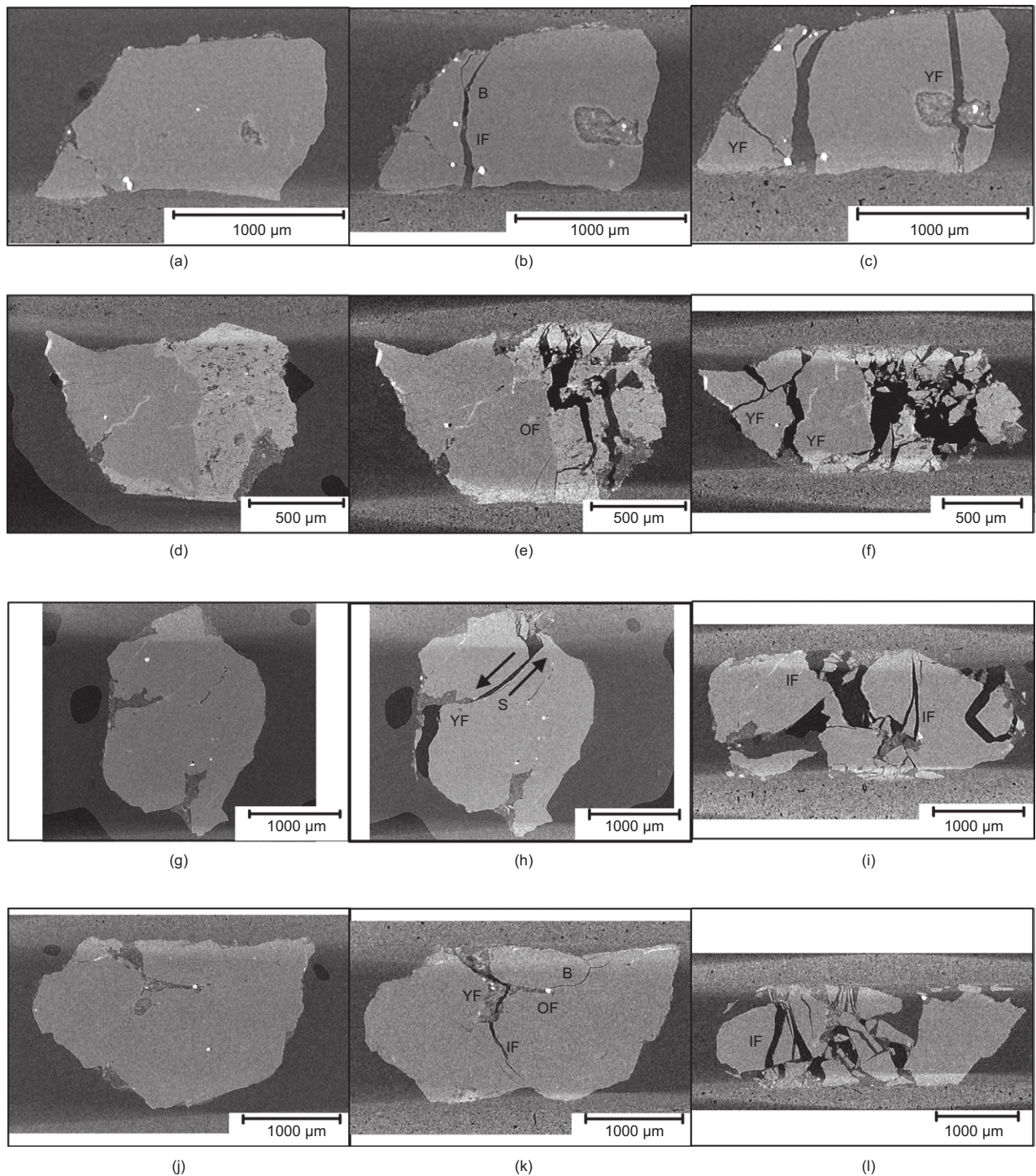


Fig. 12. Two-dimensional grey-level slices of HDG particles parallel to the loading directions: (a–c) HDG-1 at three scanning points; (d–f) HDG-2 at three scanning points; (g–i) HDG-3 at three scanning points; (j–l) HDG-4 at three scanning points (OF: original fabric related fracture; YF: young fabric related fracture; IF: fracture independent of fabric; B: bending fracture; S: shear fracture)

side (lower side) of the particle into the compression side (upper side) is marked in Fig. 12(b) (Quinn, 2007). This could be caused by the multiple lower contact points. Another example of a bending fracture is shown in Fig. 12(k). It seems that the internal weakness formed a cantilever beam, which resulted in this bending fracture. Fig. 12(h) shows a shear fracture, which made an angle of about 43° from the loading direction. The main cause for this shear fracture could be the internal weakness located at the middle of the particle. Many studies on the crushing of single sand particles between two platens are based on the hypothesis of tensile failure mode with fractures perpendicular to the loading

direction, which follows the model proposed by Jaeger (1967) for the diametrical compression of spherical rocks (Lee, 1992; McDowell & Bolton, 1998; Nakata *et al.*, 1999). This hypothesis seems not valid for some of the tested particles, especially for HDG particles with more complex external morphologies and internal microstructures.

Morphology evolution

Next, results are presented from quantitative morphological analysis of the particles and their fragments from the 3D labelled images. To present the evolution of morphology

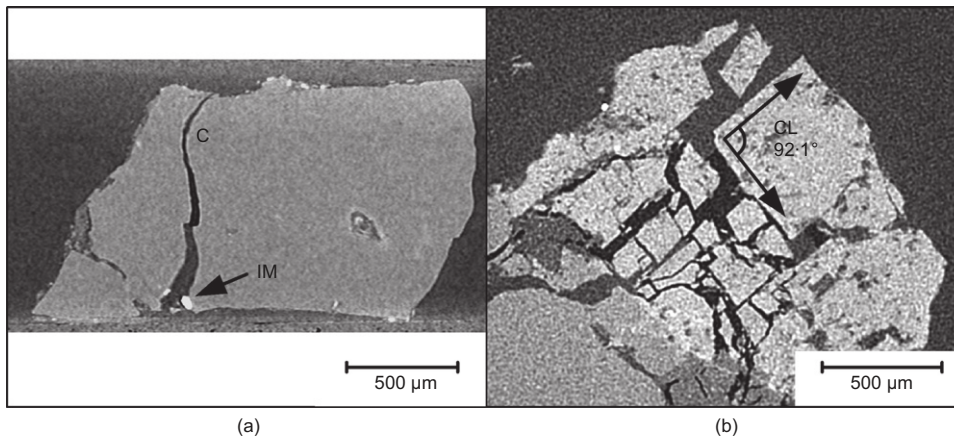


Fig. 13. Two-dimensional grey-level slices of HDG particles: (a) HDG-1 at scan 2, parallel to the loading direction; (b) HDG-3 at scan 2, perpendicular to the loading direction (C: conchoidal feature; IM: impurity; CL: fractures following cleavage)

during the fracture process, the scan results of the four particles of LBS and HDG are combined and denoted using uniform symbols. For example, 'LBS-S2' denotes all the fragments from scan 2 of the four LBS particles. Only fragments larger than 10^{-3} mm^3 (about 17 000 voxels for the largest voxel size in our test) are analysed because of the difficulties in segmenting small fragments and accurately evaluating their shape parameters. Note that each of the smallest fragments counts less than 0.05% of the total volume of the particle.

Figure 14 shows the evolution of the shape parameters for the LBS particles. Sphericity, convexity and aspect ratios tend to decrease during the particle fracture process, except for the slight increase of the flatness index (FI) from LBS-S2 to LBS-S3. This means that the newly generated fragments are less spherical, less convex and with lower aspect ratio than the original particles. Similar results have been reported by Altuhafi & Coop (2011) from one-dimensional compression on uniformly graded samples in which they used a 2D laser image analysis instrument to measure particle morphology after the tests. In spite of severe fragmentation occurring between scan 3 and scan 2, the distributions of shape parameters do not change much. The distributions of the elongation index (EI) and the flatness index (FI) for LBS-S3 are very similar, which is not surprising, given the similar physical meaning of these two parameters. It is interesting that the distributions of aspect ratios after crushing are in

agreement with the results from Takei *et al.* (2001), although they tested more angular particles. The evolution of shape parameters for the HDG particles is plotted in Fig. 15. Each line in this figure includes the morphology information of all four HDG particles. Although the HDG particles have smaller initial sphericity values than LBS particles, most fragments from both materials have a sphericity value between 0.25 and 0.65. However, the distributions of all the shape parameters of HDG particles display less difference between scan 3 and scan 2 than those of LBS particles, suggesting less variance of the fracture mechanisms of HDG particles from scan 2 to scan 3 owing to their more highly heterogeneous microstructures.

Figure 16 shows the evolution of median values of the shape parameters for the LBS and HDG particles. The median values of sphericity and convexity for both LBS and HDG particles decrease during the fracture process. Although the HDG particles have much smaller initial sphericity and convexity values than the LBS particles, they converge to the similar sphericity value of 0.51 and convexity value of 0.55. This indicates that, at the severe fragmentation level (i.e. scan 3), the median values of sphericity and convexity of the fragments are largely independent of the initial particle morphology, which is mainly resulted from the similar fracture mechanisms at this stage of fragmentation. In terms of the aspect ratios, the LBS and HDG particles have almost the same initial values of EI and FI, but the final

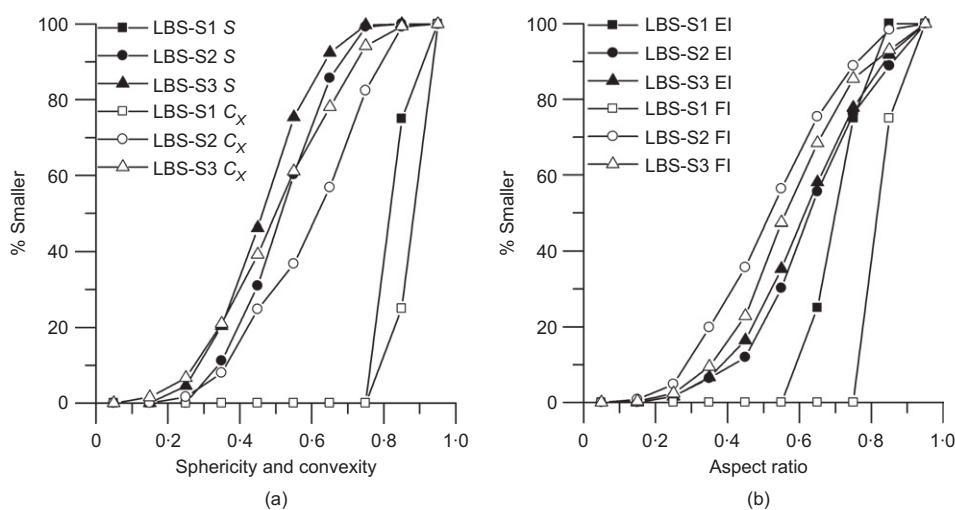


Fig. 14. Distributions of shape parameters for LBS particles at different scan stages: (a) sphericity and convexity; (b) aspect ratio. (S: sphericity; C_x: convexity; EI: elongation index; FI: flatness index)

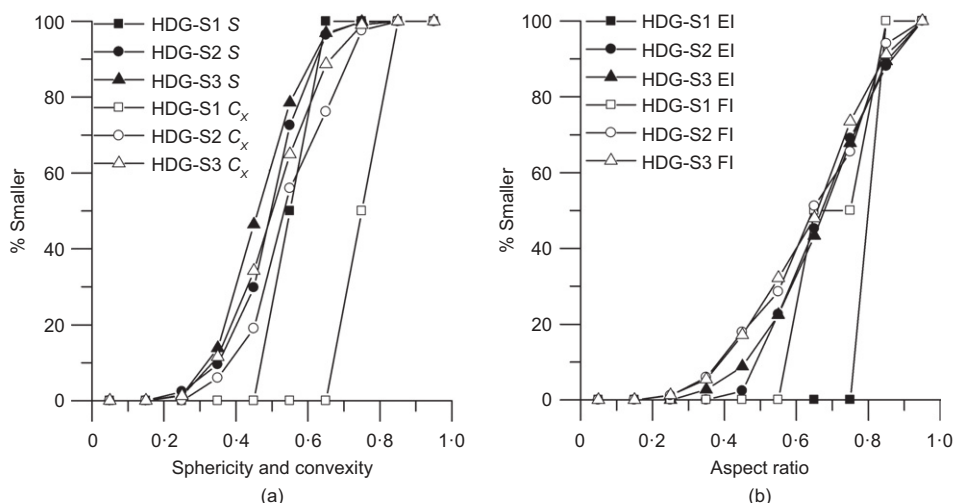


Fig. 15. Distributions of shape parameters for HDG particles at different scan stages: (a) sphericity and convexity; (b) aspect ratio (S: sphericity; C_X : convexity; EI: elongation index; FI: flatness index)

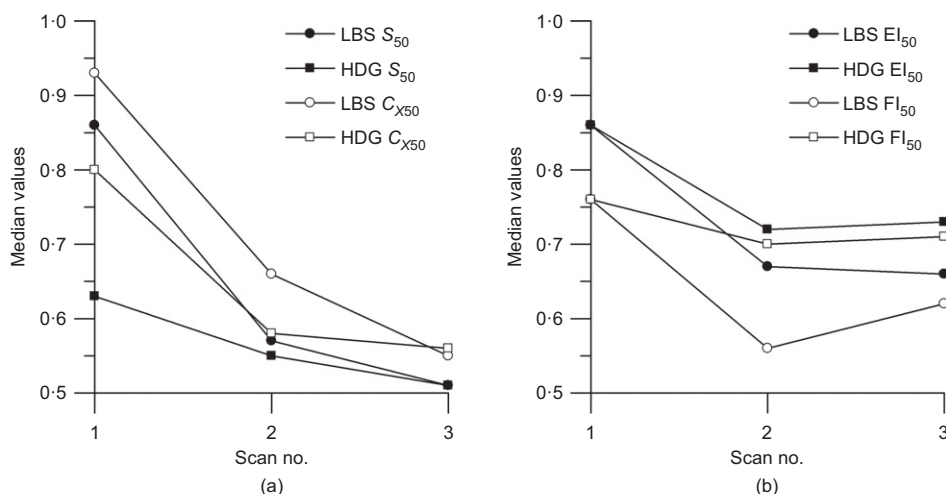


Fig. 16. Variation of median values of shape parameters during fracture: (a) sphericity and convexity; (b) aspect ratios

median values of the LBS particles are smaller than those of the HDG particles. According to the classification proposed by Zingg (1935), the median aspect ratios of the LBS fragments are 'blade', and those of the HDG fragments are 'spheroid'. Again, this result may be attributed to the more heterogeneous microstructure of the HDG particles.

By comparing the shape parameters of all the components from three scans, a strong correlation between sphericity and convexity was found in Fig. 17(a), which is in agreement with the results from Fonseca *et al.* (2012). To explore further the relationship between S and C_X , $S^{1.5}$ is calculated as the ratio between the volume of the component and the volume of the sphere having the same surface area as the component. It was found in Fig. 17(b) that the whole set of data and the correlation line shift upward above the equality line, indicating that the volume of the sphere having the same surface area as the component is larger than the volume of its convex hull. When this was not the case it was found to be caused by unsuccessfully separated fragments.

Fractal fragmentation

It has been found by many researchers that fragmentation is a scale-invariant process (Turcotte, 1986). The fractal size distributions arising from the fragmentation process have

been taken as evidence of such scale invariance. A natural material may be fragmented in a variety of ways. Weathering, explosions, impact and geological loading (e.g. basal tills sheared by glaciers) can all generate fragments that satisfy a fractal condition (Turcotte, 1986; Altuhafi & Baudet, 2011). Using the 3D morphology of the fragments from the single-particle compression tests, the present authors now examine if the fragmentation satisfies a fractal condition.

A fractal can be defined by the relationship between number and size. There are a variety of ways to represent the size–frequency distribution of fragments. Many experimental results indicate that the size–frequency distribution of fragments is given by $N \sim r^{-D}$, where N is the cumulative number of fragments with a characteristic dimension larger than r , and D is the fractal dimension corresponding to the negative slope in a $\log N(>r)$ plotted against $\log r$ plot (Turcotte, 1986).

Figure 18 shows two forms of fractal distribution of fragment size for LBS and HDG particles in scan 2 and scan 3. The particle size was described by both characteristic radius and volume. The characteristic radius is defined as the radius of a sphere that has the same volume as the fragment. It appears that the fragmentation at an extensive crushing state (scan 3) satisfies a fractal condition with a fractal dimension (D) of about 2.0 for both LBS and HDG particles.

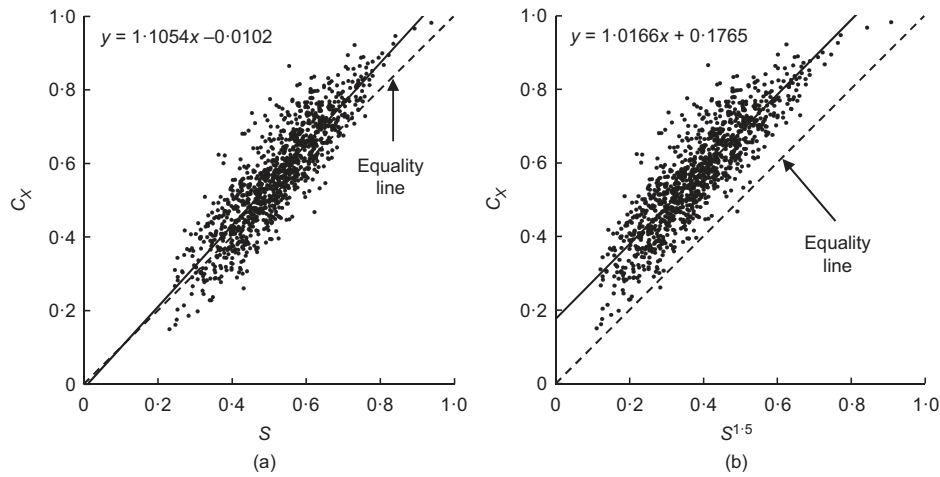


Fig. 17. Correlation between sphericity and convexity

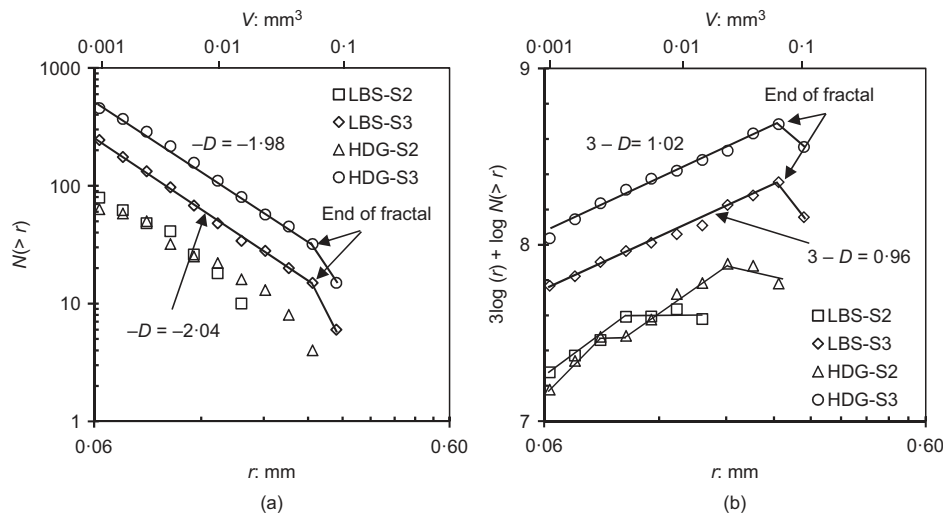


Fig. 18. The fractal distribution of fragment size: (a) $\log N(>r)$ plotted against $\log r$; (b) $3\log r + \log N(>r)$ plotted against $\log r$

Some large fragments that had not experienced significant fragmentation defined the upper end of the fractal region (Fig. 18). The lower end of the fractal range was determined by the minimum detectable volume of 10^{-3} mm^3 . Owing to the possible systematic errors in the determination of fractal dimension using the $\log(N)$ against $\log(r)$ plot (Thompson, 1991; Sufian and Russell, 2013), a second form of plotting using $3\log(r) + \log(N)$ against $\log(r)$ is given in Fig. 18(b). It is found that both plots could clearly identify the upper end of the fractal region for scan 3. For scan 2, the fractal distribution is less obvious and well defined because of the limited degree of fragmentation. However, no systematic error is found using the form of fractal plotting in Fig. 18(a). It should be mentioned that, since the volume and number of fragments were directly measured from CT data in the present study, there is no need to adopt the grain size cumulative distribution by mass such as $M_d(\leq d)/M_T = (d^{3-D} - d_{\min}^{3-D}) / (d_{\max}^{3-D} - d_{\min}^{3-D})$ suggested by Einav (2007), which can be used to back-calculate the number of fragments by assuming all particles are spherical (e.g. Zhang & Baudet, 2013).

The fractal distribution in Fig. 18 is based on the radii of equivalent spheres. This is not intended to suggest that the particle fragments are spherical, because the values of sphericity of the various sizes in Fig. 19 clearly show that they are not. Instead this is just a 'characteristic' dimension.

This approach has been used since it is not possible to reconstruct the true shape and dimension of the particles from a shape parameter such as sphericity. From Fig. 19 it is, however, clear that the mean sphericity is constant for fragment sizes below about 0.06 mm and so, whatever shape were assumed, the characteristic dimension would simply be proportional to the radius that has been used, so that the fractal dimension would not change. It is possible that the change of shape that is evident in Fig. 19 at 0.06 mm^3 may contribute to the end of the fractal domain at the same size in Fig. 18(a).

Breakage energy

The 3D geometrical information of fragments is particularly useful when coupled with load–deformation response in measuring bulk material behaviour, for example, breakage energy. There are two basic steps to measure breakage energy from the recorded data (Landis *et al.*, 2003). First, the work done by the load is calculated from load–displacement curves. The energy input is calculated as the area of the load–displacement curve during each loading period. Second, the change of surface area resulted from crack-forming processes is calculated based on the actual surface area of particles and their fragments calculated directly from the CT images. The breakage energy at any instant during the

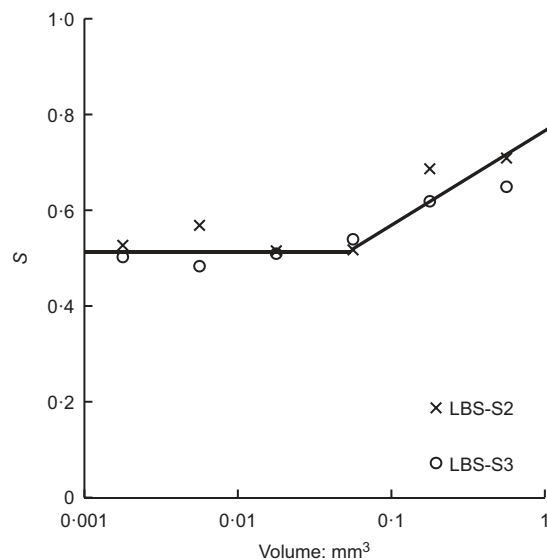


Fig. 19. Correlation between the averaged sphericity values (S) and particle size for LBS fragments at scan 2 and scan 3 in log-scale volume intervals (e.g. $(10^{-3}, 10^{-2.5}) \text{ mm}^3$, $(10^{-2.5}, 10^{-2}) \text{ mm}^3$)

loading process can then be calculated as the ratio of the incremental energy input to the incremental surface area change. It should be mentioned that the energy so calculated includes not only the energy dissipated by the creation of new surfaces during the fracture process, but also energy dissipated through other possible mechanisms like frictional dissipation between the loading platens and the particle, frictional dissipation between newly created fragments, acoustic energy. These are possible reasons why the breakage energy measured in the present study was much larger than the surface energy that Griffith used to account purely for new surface generation (Griffith, 1921). Such a definition of breakage energy is necessary because of the difficulty in distinguishing the surface energy from other forms of energy dissipation in the present experiment.

Figure 20 shows the relationship between the cumulative net work done by the load and the crack surface area measured for the LBS and HDG particles. It should be mentioned that the calculation of the cumulative net work from the load-displacement curve has excluded the amount of work consumed by the loading system, which was

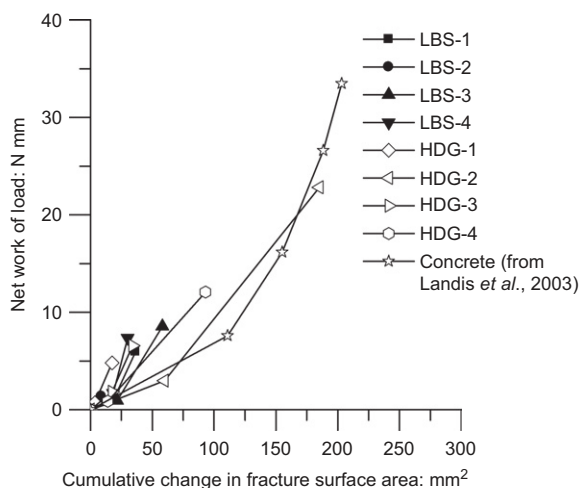


Fig. 20. Relationship between net work of load and cumulative change in surface area

calculated using an elastic stiffness of $8.07 \text{ N}/\mu\text{m}$ for the apparatus measured in a compliance test using a brass cylindrical specimen. This stiffness value is much higher than the value of $1.7 \text{ N}/\mu\text{m}$ reported by Cavarretta (2009) because the deformation of the load cell is excluded from the LVDT measurement in the current apparatus during the loading process (Fig. 1(a)). However, in an unloading event, the relaxation of the load cell and the other components of the apparatus will result in a very low unloading stiffness and the possible transfer of the energy from the loading system to the sample, which is responsible for the dynamic stress drop after the peak load seen in Fig. 8. Given this defect, the integral under the curves in Fig. 8 was taken as the upper bound of input energy. The lower bound of input energy was calculated excluding all the unloading work (i.e. areas under all unloading curves in Fig. 8). It is found that the upper bound of input work is usually twice the lower bound value. Because of the brittle failures observed in these tests, the present authors adopted the lower bound input work for the calculation of breakage energy, assuming a vertical unloading behaviour. In Fig. 20, results obtained by Landis *et al.* (2003) on concrete specimens in uniaxial compression are also plotted for comparison. Note that the concrete specimens tested by Landis *et al.* (2003) were cylinders with diameter and height both equal to 4 mm. The net work done and fracture surface area vary considerably from particle to particle. The breakage energy is calculated as the slope of each curve. The breakage energy of all the tested particles between scan 1 and scan 2 varies from 43.06 N/m to 154.49 N/m , while that between scan 2 and scan 3 is much higher, from 207.64 N/m to 484.76 N/m . The average values increase from 84.99 N/m to 321.60 N/m , which means that more energy was dissipated in generating new fractures during the second loading period. In comparison, the concrete specimens of Landis *et al.* (2003) show a larger change of the breakage energy from 68 N/m to 460 N/m . This indicates that the concrete, as a porous composite material made of aggregates and cement, is initially more fragile than natural sand particles, but becomes equally energy-dissipative at a large strain stage where severe fragmentation has occurred and energy dissipation mechanisms become more versatile.

The measured breakage energy is much larger than the surface energy, which is usually between 0.28 and 11.5 N/m for quartz and sandstone (Parks, 1984; Sufian & Russell, 2013). There are two main reasons for this large breakage energy. First, it is because the breakage energy measured includes energy dissipated through a variety of ways, as mentioned above. Second, the surface area could be greatly underestimated owing to a significant number of undetected micro-fragments and micro-cracks (Hoagland *et al.*, 1973). To illustrate the influence of the undetected small fragments in the surface area calculation, the total surface area is estimated from a fractal distribution using the same method as was used by Chester *et al.* (2005) and Russell (2014). Based on the observed fractal size distributions, a fractal dimension of 2.0 was assumed here. The number of fragments in each size interval was determined from the fractal distributions for LBS in scan 2 and scan 3, as shown in Fig. 18(a). The sphericity was used as the shape parameter to correlate volume and surface area. From Fig. 19 this was taken as 0.5 , since this value appears to be constant below about 0.06 mm^3 and so it seems reasonable to assume the same value for the undetected fragments. Then the total surface area of LBS fragments was calculated by adding up all the fragments in each size interval. It should be noted that for an assumed fractal dimension of 2.0 , the total surface area of the fragments with different characteristic sizes remains constant. Therefore, if the minimum fragment size continues to

be reduced, the estimated total surface area keeps increasing the same amount for each characteristic size. If a minimum fragment size of 10^{-12} mm³ was assumed, the resulting total surface area of LBS fragments at scan 2 and scan 3 increased 79.9% and 150.1% from that measured from X-ray CT images, respectively. Accordingly, the average breakage energy of LBS would reduce from 85.0 N/m to 36.9 N/m between scan 1 and scan 2 and from 321.6 N/m to 90.6 N/m between scan 2 and scan 3, respectively.

CONCLUSIONS

This paper has investigated the single-particle fracture behaviour of two different types of natural sand particles using a nanofocus X-ray CT. By virtue of a novel mini-loading apparatus and image-processing and analysis techniques, a detailed study has been presented on the fracture patterns, evolution of shape parameters, fractal conditions and breakage energy of a single-particle fracture event. The in-situ testing technique was particularly used in the current study to monitor closely the crushing process of sand particles and the evolving micro-morphologies of particle fragments. This has the obvious advantage over the post-mortem observation approach, which can only provide the information at the initial and the end conditions, and cannot allow the type of analysis made in this paper. The principal conclusions of this work are given below.

The initial particle morphology, heterogeneity and mineralogy are important factors that influence the fracture patterns. For the LBS particles, the fracture planes were mainly parallel to the loading direction. Local stress concentrations can occur at contact points with small radii of curvature, leading to extensive fragmentation. The initial microstructures made the particles easier to break, especially in the HDG particles. These were identified as internal voids, impurities, phase boundaries and weathering products. The fracture inside the feldspar shows a cleavage pattern, but quartz has no cleavage, so giving a conchoidal fracture when no imperfection intervenes.

The more complex external morphologies and internal microstructures led to a much richer array of fracture patterns in HDG particles. Initial structural weaknesses including internal voids, impurities, phase boundaries and weathering products resulted in the generation of different forms of tensile, shear and bending cracks through cleavage planes, mineral boundaries, voids or impurities. Obviously, these versatile fracture behaviours do not conform to the hypothesis of simple vertical splitting along the loading direction and attest to the predominant influence of particle morphology and microstructure.

Although the LBS particles had much larger sphericity and convexity values than the HDG particles, fracture caused their values to decrease and converge to the same level. In contrast, while the initial aspect ratios were similar, the final values were lower for LBS particles. The stronger LBS particles tended to produce lower aspect ratio fragments with lower angularity, but resulted in the same level of sphericity and convexity as the HDG fragments.

The fragments of both LBS and HDG particles were found to have a fractal distribution with the fractal dimension equal to about 2.0.

For both LBS and HDG particles, increasing breakage energy indicates secondary toughening mechanisms, such as frictional dissipation, gradually prevail over the energy dissipation due to crack formation. The results were found to agree well with the experimental results on a very small concrete specimen reported in the literature.

The merits of the novel insights into the single-particle fracture acquired from this study lie in the statistical

information of fragmentation morphology and its relationship with the fracture strength and energy during the fracture process. This information advances our understanding of the grain-scale fracture mechanics of natural sand particles. Although the results presented are based on only eight sand particles, many observations and insights have broad implications on the fracture behaviour of quasi-brittle geomaterials over a range of initial morphology, intrinsic microstructure and length scale, and may also shed light on the investigation of the fracture mechanics of other synthetic quasi-brittle materials such as concrete and ceramics. These results serve as the basis for further exploration of the quantitative relationship between the fracture strength of sand particles and their initial and evolving morphologies, microstructures and length scales during the crushing process in the next phase of the authors' research. Last, it should be mentioned that the major findings of this study also bear significance for numerical modelling workers, especially DEM modellers, in that the experimental observations of single-particle fracture, particularly the statistical information of the evolution of fragmentation morphology, should be considered and incorporated into the DEM model for more sophisticated modelling of sand crushing and the development of physically more robust and rigorous constitutive models for sands in future.

ACKNOWLEDGEMENTS

The study presented in this paper was supported by General Research Fund No. CityU 120512 from the Research Grant Council of the Hong Kong SAR and Research Grant No. 51379180 from the National Science Foundation of China. The authors also appreciate Dr Beatrice Baudet's discussion about the fractal plotting of particle fracture.

NOTATION

a	major dimension of component
b	intermediate dimension of component
C_X	convexity ratio between the volume of the component and its convex hull
c	minor dimension of component
D	fractal dimension corresponding to the negative slope in a log $N(>r)$ against log r plot
d_{\max}	largest particle size
d_{\min}	smallest particle size
M_d	mass of all the particles that are smaller than d
M_T	total mass of sample
N	cumulative number of fragments with a characteristic dimension larger than r
Ra	parameter of surface roughness
S	sphericity
V	volume of component
V_{CH}	volume of the convex hull enclosing component

REFERENCES

- Alshibli, K. A., Sture, S., Costes, N. C., Frank, M. L., Lankton, M. R., Batiste, S. N. & Swanson, R. A. (2000). Assessment of localized deformations in sand using X-ray computed tomography. *ASTM Geotech. Testing J.* **23**, No. 3, 274–299.
- Altuhafi, F. & Baudet, B. A. (2011). A hypothesis on the relative roles of crushing and abrasion in the mechanical genesis of a glacial sediment. *Engng Geol.* **120**, No. 1, 1–9.
- Altuhafi, F. N. & Coop, M. R. (2011). Changes to particle characteristics associated with the compression of sands. *Géotechnique* **61**, No. 6, 459–471, <http://dx.doi.org/10.1680/geot.9.P114>.
- Andò, E., Viggiani, G., Hall, S. & Desrues, J. (2013). Experimental micro-mechanics of granular media studied by X-ray

- tomography: recent results and challenges. *Géotechnique Lett.* **3**, No. 3, 142–146.
- Barrett, P. J. (1980). The shape of rock particles, a critical review. *Sedimentology* **27**, No. 3, 291–303.
- Beucher, S. & Lantuejoul, C. (1979). Use of watersheds in contour detection. *Proceedings of the international workshop on image processing, real-time edge and motion detection/estimation*, Rennes, France.
- Bolton, M. D., Nakata, Y. & Cheng, Y. P. (2008). Micro-and macro-mechanical behaviour of DEM crushable materials. *Géotechnique* **58**, No. 6, 471–480, <http://dx.doi.org/10.1680/geot.2008.58.6.471>.
- Brzesowsky, R. H., Spiers, C. J., Peach, C. J. & Hangx, S. J. T. (2011). Failure behavior of single sand grains: theory versus experiment. *J. Geophys. Res.: Solid Earth (1978–2012)*, **116**, No. 6, B06205/1–B06205/13.
- Cavarretta, I. (2009). *The influence of particle characteristics on the engineering behaviour of granular materials*. PhD thesis, Imperial College London, London, UK.
- Cavarretta, I. & O'Sullivan, C. (2012). The mechanics of rigid irregular particles subject to uniaxial compression. *Géotechnique* **62**, No. 8, 681–692, <http://dx.doi.org/10.1680/geot.10.P102>.
- Cavarretta, I., Coop, M. R. & O'Sullivan, C. (2010). The influence of particle characteristics on the behaviour of coarse grained soils. *Géotechnique* **60**, No. 6, 413–423, <http://dx.doi.org/10.1680/geot.2010.60.6.413>.
- Cheng, Y. P., Nakata, Y. & Bolton, M. D. (2003). Discrete element simulation of crushable soil. *Géotechnique* **53**, No. 7, 633–641, <http://dx.doi.org/10.1680/geot.2003.53.7.633>.
- Chester, J. S., Chester, F. M. & Kronenberg, A. K. (2005). Fracture surface energy of the Punchbowl fault, San Andreas system. *Nature* **437**, No. 7055, 133–136.
- Cho, G. C., Dodds, J. & Santamarina, J. C. (2006). Particle shape effects on packing density, stiffness, and strength: natural and crushed sands. *J. Geotech. Geoenviron. Engng* **132**, No. 5, 591–602.
- Cil, M. B. & Alshibli, K. A. (2012). 3D assessment of fracture of sand particles using discrete element method. *Géotechnique Lett.* **2**, No. 3, 161–166.
- Cil, M. B. & Alshibli, K. A. (2014). 3D evolution of sand fracture under 1D compression. *Géotechnique* **64**, No. 5, 351–364, <http://dx.doi.org/10.1680/geot.13.P119>.
- Coop, M. R., Sorensen, K. K., Freitas, T. B. & Georgoutsos, G. (2004). Particle breakage during shearing of a carbonate sand. *Géotechnique* **54**, No. 3, 157–163, <http://dx.doi.org/10.1680/geot.2004.54.3.157>.
- Davis, G. R. & Elliott, J. C. (2006). Artefacts in X-ray microtomography of materials. *Mater. Sci. Technol.* **22**, No. 9, 1011–1018.
- Deng, G. & Cahill, L. W. (1993). An adaptive Gaussian filter for noise reduction and edge detection. *Proceedings of the nuclear science symposium and medical imaging conference, IEEE conference record*, San Francisco, CA, vol. 3, pp. 1615–1619.
- Desrues, J., Chambon, R., Mokni, M. & Mazerolle, F. (1996). Void ratio evolution inside shear bands in triaxial sand specimens studied by computed tomography. *Géotechnique* **46**, No. 3, 529–546, <http://dx.doi.org/10.1680/geot.1996.46.3.529>.
- Einav, I. (2007). Breakage mechanics—part 1: theory. *J. Mech. Phys. Solids* **55**, No. 6, 1274–1297.
- Fonseca, J. (2011). *The evolution of morphology and fabric of a sand during shearing*. PhD thesis, Imperial College London, London, UK.
- Fonseca, J., O'Sullivan, C., Coop, M. R. & Lee, P. D. (2012). Non-invasive characterization of particle morphology of natural sands. *Soils Found.* **52**, No. 4, 712–722.
- Fonseca, J., O'Sullivan, C., Coop, M. R. & Lee, P. D. (2013). Quantifying the evolution of soil fabric during shearing using directional parameters. *Géotechnique* **63**, No. 6, 487–499, <http://dx.doi.org/10.1680/geot.12.P003>.
- Gallagher, J. J. (1987). Fractography of sand grains broken by uniaxial compression. In *Clastic particles: scanning electron microscopy and shape analysis of sedimentary and volcanic clasts* (ed. J. R. Marshall), pp. 189–228. New York, USA: Van Nostrand Reinhold.
- Geotechnical Control Office (1984). *Geotechnical manual for slopes*, 2nd edn. Hong Kong: Geotechnical Control Office.
- Gonzalez, R. C. & Woods, R. E. (2010). *Digital image processing*. Upper Saddle River, NJ, USA: Pearson/Prentice Hall.
- Griffith, A. A. (1921). The phenomena of rupture and flow in solids. *Phil. Trans. R. Soc. London Ser. A* **221**, 163–198.
- Hall, S. A., Bornert, M., Desrues, J., Pannier, Y., Lenoir, N., Viggiani, G. & Bésuelle, P. (2010). Discrete and continuum analysis of localised deformation in sand using X-ray μ CT and volumetric digital image correlation. *Géotechnique* **60**, No. 5, 315–322, <http://dx.doi.org/10.1680/geot.2010.60.5.315>.
- Hanley, K. J., O'Sullivan, C., Oliveira, J. C., Cronin, K. & Byrne, E. P. (2011). Application of Taguchi methods to DEM calibration of bonded agglomerates. *Powder Technol.* **210**, No. 3, 230–240.
- Hoagland, R. G., Hahn, G. T. & Rosenfield, A. R. (1973). Influence of microstructure on fracture propagation in rock. *Rock Mech.* **5**, No. 2, 77–106.
- Hodson, E. K., Thayer, D. & Franklin, C. (1981). Adaptive Gaussian filtering and local frequency estimates using local curvature analysis. *Acoustics, Speech and Signal Processing, IEEE Trans.* **29**, No. 4, 854–859.
- Jaeger, J. C. (1967). Failure of rocks under tensile conditions. *Int. J. Rock Mech. Mining Sci. Geomech. Abstracts* **4**, No. 2, 219–227.
- Landis, E. N., Nagy, E. N. & Keane, D. T. (2003). Microstructure and fracture in three dimensions. *Engng Fracture Mech.* **70**, No. 7, 911–925.
- Lee, D. M. (1992). *The angles of friction of granular fills*. PhD thesis, University of Cambridge, Cambridge, UK.
- Lee, I. K. & Coop, M. R. (1995). The intrinsic behaviour of a decomposed granite soil. *Géotechnique* **45**, No. 1, 117–130, <http://dx.doi.org/10.1680/geot.1995.45.1.117>.
- Lindblad, J. (2005). Surface area estimation of digitized 3D objects using weighted local configurations. *Image Vision Comput.* **23**, No. 2, 111–122.
- Lobo-Guerrero, S. & Vallejo, L. E. (2005). DEM analysis of crushing around driven piles in granular materials. *Géotechnique* **55**, No. 8, 617–623, <http://dx.doi.org/10.1680/geot.2005.55.8.617>.
- McDowell, G. R. (2002). On the yielding and plastic compression of sand. *Soils Found.* **42**, No. 1, 139–145.
- McDowell, G. R. (2005). A physical justification for log e –log σ based on fractal crushing and particle kinematics. *Géotechnique* **55**, No. 9, 697–698, <http://dx.doi.org/10.1680/geot.2005.55.9.697>.
- McDowell, G. R. & Amon, A. (2000). The application of Weibull statistics to the fracture of soil particles. *Soils Found.* **40**, No. 5, 133–141.
- McDowell, G. R. & Bolton, M. D. (1998). On the micromechanics of crushable aggregates. *Géotechnique* **48**, No. 5, 667–679, <http://dx.doi.org/10.1680/geot.1998.48.5.667>.
- McDowell, G. R. & Harireche, O. (2002). Discrete element modelling of soil particle fracture. *Géotechnique* **52**, No. 2, 131–135, <http://dx.doi.org/10.1680/geot.2002.52.2.131>.
- McDowell, G. R., Bolton, M. D. & Robertson, D. (1996). The fractal crushing of granular materials. *J. Mech. Phys. Solids* **44**, No. 12, 2079–2101.
- Nakata, Y., Hyde, A. F. L., Hyodo, M. & Murata, H. (1999). A probabilistic approach to sand particle crushing in the triaxial test. *Géotechnique* **49**, No. 5, 567–583, <http://dx.doi.org/10.1680/geot.1999.49.5.567>.
- Nakata, Y., Kato, Y., Hyodo, M., Hyde, A. F. L. & Murata, H. (2001). One-dimensional compression behaviour of uniformly graded sand related to single particle crushing strength. *Soils Found.* **41**, No. 2, 39–51.
- Otsu, N. (1979). A threshold selection method from gray-level histograms. *IEEE Trans. Systems, Man Cybernet.* **9**, No. 1, 62–66.
- Parks, G. A. (1984). Surface and interfacial free energies of quartz. *J. Geophys. Res.: Solid Earth (1978–2012)* **89**, No. B6, 3997–4008.
- Phillion, A. B., Lee, P. D., Maire, E. & Cockcroft, S. L. (2008). Quantitative assessment of deformation-induced damage in a semisolid aluminum alloy via X-ray microtomography. *Metall. Mater. Trans. A* **39**, No. 10, 2459–2469.
- Quinn, G. D. (2007). *Fractography of ceramics and glasses*, NIST Special Publication 960-16. Gaithersburg, MD, USA: National Institute of Standards and Technology (NIST).

- Robertson, D. (2000). *Numerical simulations of crushable aggregates*. PhD thesis, University of Cambridge, Cambridge, UK.
- Russell, A. R. (2011). A compression line for soils with evolving particle and pore size distributions due to particle crushing. *Géotechnique Lett.* **1**, No. 1, 5–9.
- Russell, A. R. (2014). How water retention in fractal soils depends on particle and pore sizes, shapes, volumes and surface areas. *Géotechnique* **64**, No. 5, 379–390, <http://dx.doi.org/10.1680/geot.13.P165>.
- Russell, A. R. & Einav, I. (2013). Energy dissipation from particulate systems undergoing a single particle crushing event. *Granular Matter* **15**, No. 3, 299–314.
- Russell, A. R. & Muir Wood, D. (2009). Point load tests and strength measurements for brittle spheres. *Int. J. Rock Mech. Mining Sci.* **46**, No. 2, 272–280.
- Stock, S. R. (2008). Recent advances in X-ray microtomography applied to materials. *Int. Mater. Rev.* **53**, No. 3, 129–181.
- Sufian, A. & Russell, A. R. (2013). Microstructural pore changes and energy dissipation in Gosford sandstone during pre-failure loading using X-ray CT. *Int. J. Rock Mech. Mining Sci.* **57**, 119–131.
- Takei, M., Kusakabe, O. & Hayashi, T. (2001). Time-dependent behavior of crushable materials in one-dimensional compression tests. *Soils Found.* **41**, No. 1, 97–121.
- Tarantino, A. & Hyde, A. F. L. (2005). An experimental investigation of work dissipation in crushable materials. *Géotechnique* **55**, No. 8, 575–584, <http://dx.doi.org/10.1680/geot.2005.55.8.575>.
- Thompson, A. H. (1991). Fractals in rock physics. *Ann. Rev. Earth Planetary Sci.* **19**, No. 1, 237–262.
- Turcotte, D. L. (1986). Fractals and fragmentation. *J. Geophys. Res.: Solid Earth (1978–2012)* **91**, No. B2, 1921–1926.
- Wadell, H. (1932). Volume, shape, and roundness of rock particles. *J. Geol.* **40**, No. 5, 443–451.
- Wählby, C., Sintorn, I. M., Erlandsson, F., Borgefors, G. & Bengtsson, E. (2004). Combining intensity, edge and shape information for 2D and 3D segmentation of cell nuclei in tissue sections. *J. Microscopy* **215**, No. 1, 67–76.
- Wang, J. & Yan, H. (2012). DEM analysis of energy dissipation in crushable soils. *Soils Found.* **52**, No. 4, 644–657.
- Wang, J. & Yan, H. (2013). On the role of particle breakage in the shear failure behavior of granular soils by DEM. *Int. J. Numer. Analyt. Methods Geomech.* **37**, No. 8, 832–854.
- Yoshimoto, N., Hyodo, M., Nakata, Y., Orense, R. P., Hongo, T. & Ohnaka, A. (2012). Evaluation of shear strength and mechanical properties of granulated coal ash based on single particle strength. *Soils Found.* **52**, No. 2, 321–334.
- Zhang, X. & Baudet, B. A. (2013). Particle breakage in gap-graded soil. *Géotechnique Lett.* **3**, No. 2, 72–77.
- Zingg, T. (1935). Beitrag zur Schotteranalyse. *Schweizerische Mineralogische und Petrographische Mitteilungen* **15**, 52–56 (in German).